

# Detailed 3D Seismic Velocity Structure of the Prague, Oklahoma Fault Zone and the Implications for Induced Seismicity

Lipeng He<sup>1</sup>, Qimin Wu<sup>2</sup>, Xiaowei Chen<sup>3</sup>, Xinlei Sun<sup>4</sup>, Zhen Guo<sup>1</sup>, and Yongshun Chen<sup>1</sup>

<sup>1</sup>Southern University of Science and Technology

<sup>2</sup>Lettis Consultants International, Inc.

<sup>3</sup>University of Oklahoma

<sup>4</sup>Chengdu University of Technology

November 22, 2022

## Abstract

The 2011 Mw 5.7 Prague earthquake is the second largest induced earthquake in Oklahoma, and occurred after decades of wastewater disposal. The local geological structure that led to the triggering of this large earthquake is not well understood. In this study, tomographic inversion of seismic data recorded by a dense local seismic network resulted in a high-resolution 3D velocity model with three major layers. The model clearly illuminates the geometry and characteristics of the Meeker-Prague Fault that hosted the 2011 Prague sequence. A conceptual model is proposed to link the tomographic structure to the triggering process of the sequence. The low-permeability second layer at ~1.5-3.5 km may be the key that delays the occurrence of the first sizeable earthquake after decades of wastewater injection. However, a low-shear-velocity zone within this layer at the intersection of two major faults could have provided a fluid pathway to facilitate downward fluid propagation.

1 **Detailed 3D Seismic Velocity Structure of the Prague, Oklahoma Fault Zone and the**  
2 **Implications for Induced Seismicity**

3 **Lipeng He<sup>1,2</sup>, Qimin Wu<sup>1,3,\*</sup>, Xiaowei Chen<sup>1</sup>, Xinlei Sun<sup>4</sup>, Zhen Guo<sup>2</sup> and Yongshun John**  
4 **Chen<sup>2,\*</sup>**

5 <sup>1</sup>School of Geosciences, University of Oklahoma, Norman, OK, USA.

6 <sup>2</sup>Department of Ocean Science and Engineering, Southern University of Science and  
7 Technology, Shenzhen, Guangdong, China.

8 <sup>3</sup>Lettis Consultants International, Inc., Concord, CA, USA.

9 <sup>4</sup>International Center for Planetary Science, College of Geosciences, Chengdu University of  
10 Technology

11  
12 Corresponding authors: Qimin Wu ([wu@lettisci.com](mailto:wu@lettisci.com)), Yongshun John Chen  
13 ([johnc@ustech.edu.cn](mailto:johnc@ustech.edu.cn))

14  
15 **Key Points:**

- 16 • We develop a fine fault zone velocity structure for the 2011 Mw 5.7 Prague earthquake  
17 and relocate the earthquakes using the 3D models.
- 18 • The results depict the Meeker-Prague Fault that hosted the majority of the larger events in  
19 the Prague sequence.
- 20 • We propose a conceptual model that links velocity structure to the triggering process of the  
21 Prague sequence due to wastewater injection.

## 22 **Abstract**

23 The 2011 Mw 5.7 Prague earthquake is the second largest induced earthquake in Oklahoma, and  
24 occurred after decades of wastewater disposal. The local geological structure that led to the  
25 triggering of this large earthquake is not well understood. In this study, tomographic inversion of  
26 seismic data recorded by a dense local seismic network resulted in a high-resolution 3D velocity  
27 model with three major layers. The model clearly illuminates the geometry and characteristics of  
28 the Meeker-Prague Fault that hosted the 2011 Prague sequence. A conceptual model is proposed  
29 to link the tomographic structure to the triggering process of the sequence. The low-permeability  
30 second layer at ~1.5-3.5 km may be the key that delays the occurrence of the first sizeable  
31 earthquake after decades of wastewater injection. However, a low-shear-velocity zone within this  
32 layer at the intersection of two major faults could have provided a fluid pathway to facilitate  
33 downward fluid propagation.

## 34 **Plain Language Summary**

35 The recent surge of seismicity in the central United States since 2008 has largely been attributed  
36 to wastewater disposal from oil and gas production. The 6 November 2011 Mw 5.7 earthquake  
37 near Prague, is the second largest earthquake ever recorded instrumentally in the state of  
38 Oklahoma. Previous studies mainly focused on the characterization of seismicity in the 2011  
39 Prague earthquake sequence and found that the majority of earthquakes occurred along the  
40 Meeker-Prague fault, which is a ~20 km splay fault off the Wilzetta fault zone. In this study, we  
41 apply the seismic traveltime tomography technique on data recorded by a dense local seismograph  
42 network to image the fine upper crustal velocity structure in the Prague fault zone. Our results  
43 clearly mapped zones with significant velocity anomalies in the fault zone compared to the  
44 surrounding area. And the velocity anomalies coincide with the clusters of seismicity, indicating  
45 that fluid injection probably played an important role in altering the properties of the fault zone  
46 and therefore promoting the occurrence of earthquakes. This study highlights that it is critical to  
47 investigate the fault zone structure to advance our understanding of the process of pore pressure  
48 diffusion and fluid migration in triggering of induced seismicity.

## 49 **1 Introduction**

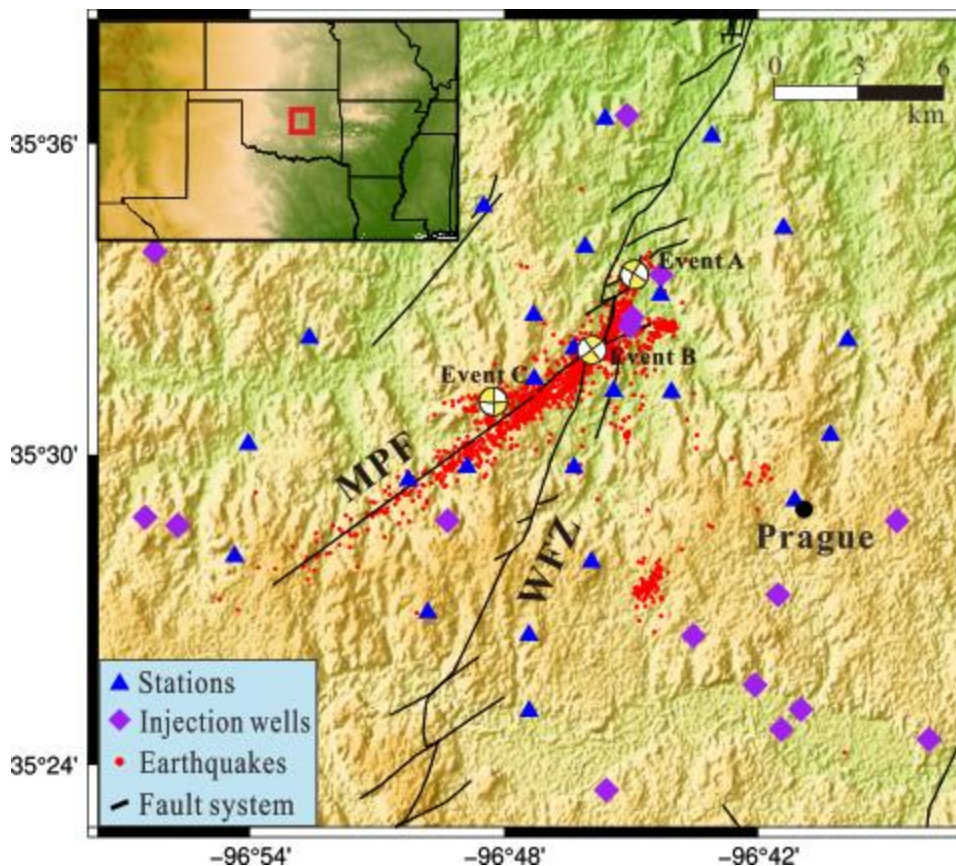
50 The unprecedented increase in the seismicity rate in the central United States (CUS) since  
51 2008 has largely been attributed to the large volume of wastewater disposal from oil and gas  
52 production (Ellsworth, 2013; Keranen & Weingarten, 2018). In Oklahoma, several significant  
53 induced earthquakes have occurred since 2011, including the 2011 Mw 5.7 Prague earthquake and  
54 the 2016 Mw 5.8 Pawnee earthquake, both of which caused considerable damage in the epicentral  
55 regions (Keranen et al., 2013; Yeck et al., 2016). Although the earthquake rate has been declining  
56 in Oklahoma since 2016, in part due to mandated reductions in rates for wastewater injection  
57 (Stewart & Ingelson, 2017), it remains well above background levels and puts the state at an  
58 elevated level of seismic hazards (Langenbruch & Zoback, 2016; Petersen et al., 2016; Petersen et  
59 al., 2017; Petersen et al., 2018).

60 It is generally accepted that the increase in pore fluid pressure associated with wastewater  
61 injection reduces the frictional resistance on pre-existing fault planes and thus promotes their  
62 reactivation. The fact that not all wells with high wastewater injection rates are linked to induced  
63 earthquakes, and that sometimes earthquakes occur near wells with low injection rates, indicates  
64 that induced seismicity depends both on the injection parameters and on the local geological

65 structures (Schultz et al., 2016; Shah & Keller, 2017). Regional studies on the crustal structures in  
66 Oklahoma indicate that moderate earthquakes tend to occur close to the boundaries of high- and  
67 low-seismic velocity zones that are interpreted as geological boundaries of different basement rock  
68 properties (Pei et al., 2018; Chai et al., 2021). The hydrological structure of the subsurface is  
69 important in controlling the spatial and temporal distributions of fluid pressure perturbations in the  
70 subsurface. Highly permeable fault zones facilitate pore pressure propagation and channel fluid  
71 flow to travel large distances from injection wells, potentially reaching critically stressed basement  
72 faults (e.g., Chiarabba et al., 2018; Shah & Keller, 2017). It is therefore critical to identify the  
73 structures that control pore pressure diffusion and fluid migration toward large active faults in  
74 order to advance our understanding of the triggering mechanisms of induced seismicity.

75 The 2011 Mw 5.7 Prague earthquake sequence was the first significant earthquake  
76 sequence that has been attributed to wastewater disposal in Oklahoma, which ruptured a previously  
77 unmapped portion of the Wilzetta Fault zone (WFZ) (Figure 1, Keranen et al., 2013; McMahan et  
78 al., 2017). The relocated seismicity and focal mechanisms suggest a complex fault zone with three  
79 primary faults, as defined by the Mw 4.8 foreshock, the Mw 5.7 mainshock, and the Mw 4.8  
80 aftershock, respectively (Cochran et al., 2020; Keranen et al., 2013; McMahan et al., 2017;  
81 Pennington et al., 2021). Seismological analysis suggests that the Mw 5.7 mainshock ruptured an  
82 unmapped Meeker-Prague Fault (MPF, McMahan et al., 2017) that is optimally oriented in the  
83 stress field (Cochran et al., 2020). The onset of induced earthquakes is commonly observed soon  
84 after the initiation of fluid injection (e.g., Frohlich et al., 2011; Horton, 2012; Tan et al., 2020).  
85 However, the first notable earthquake (i.e., the Mw 4.8 foreshock) near Prague did not occur until  
86 18 years after injection had commenced, and there is no clear temporal correlation between  
87 changes in wastewater disposal rates at the wells and the timing of the Prague sequence in late  
88 2011 (Walsh & Zoback, 2015). The coseismic rupture of the Mw 5.7 mainshock is considerably  
89 heterogeneous consisting of multiple slip patches at depths ~3-9 km (Sun & Hartzell, 2014),  
90 indicating variable fault strength and stress conditions on the fault, which is consistent with the  
91 strong variability of stress drop estimates for the sequence (Pennington et al., 2021; Sumy et al.,  
92 2017; Wu et al., 2018). In addition, stress field analysis by Cochran et al. (2020) demonstrates that  
93 both optimally and unfavorably oriented faults were activated during the 2011 Prague sequence,  
94 which highlights the complex structure of the fault zone, as well as the significance of pore  
95 pressure changes in promoting the failure of the unfavorably oriented faults, in addition to the  
96 triggering by earthquake interaction through Coulomb stress transfer (e.g., Chen et al., 2017; Sumy  
97 et al., 2014). However, the mechanism that controls the timing and detailed failure process of the  
98 2011 sequence and the relative contributions of fault zone structures and pore pressure changes  
99 due to injection remain unclear.

100 To shed light on the aforementioned scientific questions, in this study, we focus on the fine  
101 3D structure of the fault system, and the role of fluids in the evolution of the Prague sequence. The  
102 new results presented here allow us to evaluate the link between the fault zone structure and the  
103 evolution of seismicity, providing new insights on the triggering processes of induced seismicity.



104  
 105 **Figure 1.** Topographic map of the Prague, Oklahoma. Inset map shows the location of the study  
 106 area (red rectangle). Faults are marked with black solid lines. Blue triangles show the seismic  
 107 stations and purple diamonds represent the wastewater injection wells. MPF: Meeker-Prague Fault,  
 108 WFZ: Wilzetta Fault zone. Event A, B and C represent the Mw 4.8 foreshock (5 November 2011),  
 109 the Mw 5.7 mainshock (6 November 2011) and the Mw 4.8 aftershock (8 November 2011),  
 110 respectively (locations from USGS). Red dots denote the 1508 earthquake locations from the  
 111 catalog by McMahon et al. (2017) between November 2011 and April 2012.

## 112 2 Data and Methods

113 Shortly after the Mw 4.8 foreshock on 5 November 2011, teams from the Program for  
 114 Array Seismic Studies of the Continental Lithosphere (PASSCAL), Rapid Array Mobilization  
 115 Program (RAMP), the University of Oklahoma (OU), and the United States Geological Survey  
 116 (USGS) deployed 31 three-component temporary seismometers to monitor the following seismic  
 117 activity near Prague (Figure 1, Sumy et al., 2014). We selected a subset of 1508 well-recorded  
 118 earthquakes that were recorded by at least 5 stations from the template-matching derived catalog  
 119 by McMahon et al. (2017), and manually picked P and S wave arrivals. We only used earthquakes  
 120 with both P and S phase picks at five or more stations to facilitate a better comparison between  $V_p$   
 121 and  $V_s$ , and to ensure the reliability of the  $V_p/V_s$  (Zenonos et al., 2020). To further filter out low-  
 122 quality data, we evaluated the distribution of the P and S wave travel times versus distance and  
 123 fitted the data using least squares linear regression (Figure S1). Traveltime data that fall outside  
 124 two standard deviations about the linear trend were considered outliers and were eliminated.  
 125 Finally, we obtained 18,900 P wave and 18,900 S wave arrival times for further analyses.

126 We first use the HypoDD program (Waldhauser & Ellsworth, 2000; Figure S2, Text S1) to  
127 relocate the selected earthquakes using a 1D velocity model of Prague (Keranen et al., 2013), and  
128 then invert the selected P wave and S wave arrival times for 3D velocity models. The ray-paths for  
129 all data used in the tomography are presented in Figure S3. We adopt the Fast Marching  
130 tomography algorithm (FMTOMO, de Kool et al., 2006; Rawlinson et al., 2006, Text S2) to invert  
131 for both the Vp and Vs structures. For the determination of the Vp/Vs model, instead of simply  
132 taking the ratio of Vp and Vs models, we apply a modified version of the FMTOMO code to  
133 directly invert for Vp/Vs using S-P times following Zenonos et al. (2020), which has been  
134 demonstrated to produce more robust Vp/Vs model. The region of interest in this study is  
135 approximately 40 km (EW direction) by 30 km (NS direction), and extends from the ground  
136 surface to 16 km depth. The inversion converged after six iterations, and the root-mean-square of  
137 the traveltimes residuals was reduced from 0.43 to 0.23 s for P arrivals and from 0.65 to 0.24 s for  
138 S arrivals for the final velocity model. Figure S4 shows the traveltimes residuals after inversion for  
139 both P- and S-waves. The residuals are centered at 0 s with the majority falling within the range  
140 of -0.2 to 0.2 s, suggesting that the final model predicts the traveltimes quite well. Lastly, we  
141 relocate the earthquakes using our inverted 3D velocity models and the 3D version of HypoDD.

142 We perform checkerboard tests to evaluate the resolution of the 3D velocity models. In the  
143 checkerboard resolution tests, we set the input velocity perturbations at  $\pm 0.5$  km/s relative to the  
144 reference model. The spatial resolution is about 2.5 km in both horizontal and vertical directions  
145 based on the results of the checkerboard tests. Figure S5, S6 and S7 show depth slices and cross-  
146 sectional views of the recovered models for Vp, Vs and Vp/Vs, respectively. These figures suggest  
147 that the models are well resolved at depths of 0-8 km.

### 148 **3 Results**

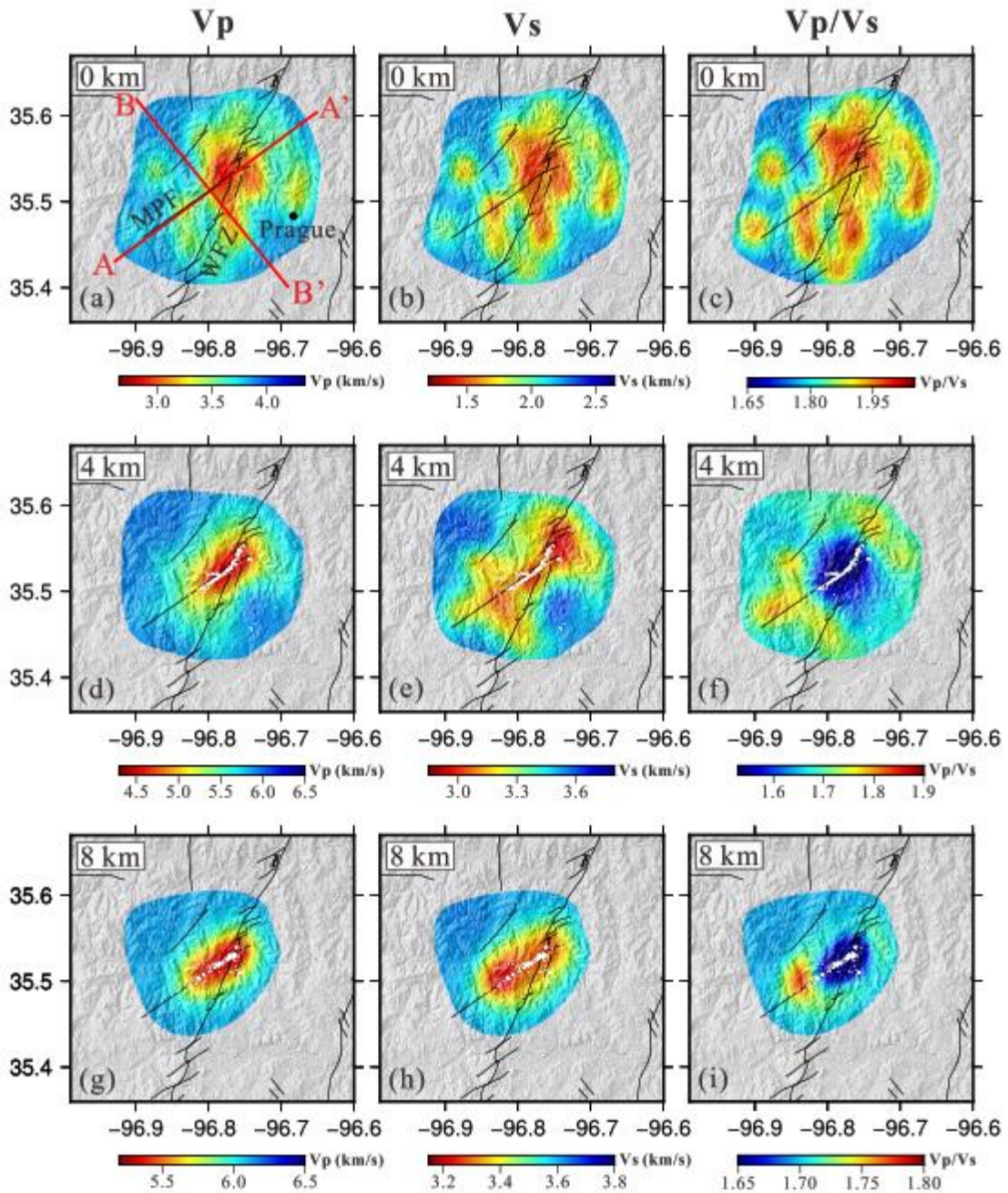
149 Figure 2 shows horizontal slices of Vp (left), Vs (middle), and Vp/Vs (right) models at  
150 various depths. In general, Vp and Vs models show similar patterns. At the surface (Figure 2a, b,  
151 c), low velocities with high Vp/Vs spread widely, including within the WFZ and along the MPF.  
152 The widespread low velocities near the surface are associated with the sedimentary layer in this  
153 region. In contrast, the low velocity anomalies at 4 km depth show more concentrated pattern that  
154 generally follows the trend of the MPF, and almost all earthquakes at this depth occurred within  
155 the low velocity zones (Figures 2d, e), which correlate remarkably well with the region of low  
156 Vp/Vs anomalies (Figure 2f). Similarly, a low Vp/Vs zone at 8 km depth correlates well with the  
157 low velocity anomalies and follows the trend of the MPF (Figure 2g, h and i). Notably, the most  
158 significant velocity anomalies, particularly Vp/Vs, occur at the intersection of WFZ and MPF  
159 (Figure 2), where the Mw 5.7 mainshock and the Mw 4.8 foreshock are located.

160 Figure 3 shows cross sections for the resulting Vp (Figures 3a, b), Vs (Figures 3c, d), and  
161 Vp/Vs (Figures 3e, f) models along two orthogonal profiles with profile AA' trending NE-SW  
162 along the MPF (Figure 2a). Based on the velocity profiles, we infer three layers in the fault zone  
163 with distinct velocity characteristics (Figure 3c).

164 The sedimentary layer is clearly outlined by low Vp and Vs at depths shallower than  $\sim 1.5$   
165 km across the entire study area ("Layer 1" in Figure 3c). This layer is also associated with high  
166 Vp/Vs, particularly around the fault zone (Figures 3e, f). The bottom of this layer varies at depth  
167 from about 1 to 2 km, consistent with the depth to the Arbuckle and Hunton formations obtained  
168 from well logs and electrical logs (Pennington et al., 2021). At "Layer 2" (Figure 3c), between  
169  $\sim 1.5$ -3.5 km depth, the models are characterized by Vp and Vs with moderate velocity values and

170 relatively normal  $V_p/V_s$ . A notable low  $V_s$  anomaly (marked as "LSV" in Figure 3c) exists near  
171 the northeast end of the seismicity volume in "Layer 2", which connects the "Layer 1" and "Layer  
172 3". "Layer 3", which is located right below the Arbuckle formation in the basement and hosted a  
173 majority of events including the Mw 5.7 mainshock, exhibits remarkable low  $V_p$  and  $V_s$  along  
174 with anomalously low  $V_p/V_s$  (Figure 3). Figure S8 shows three representative 1D vertical profiles  
175 along cross section AA' including one background profile, a second going through the low  $V_s$   
176 anomaly LSV, and the third going through the low-velocity anomaly in Layer 3 but does not pass  
177 LSV.

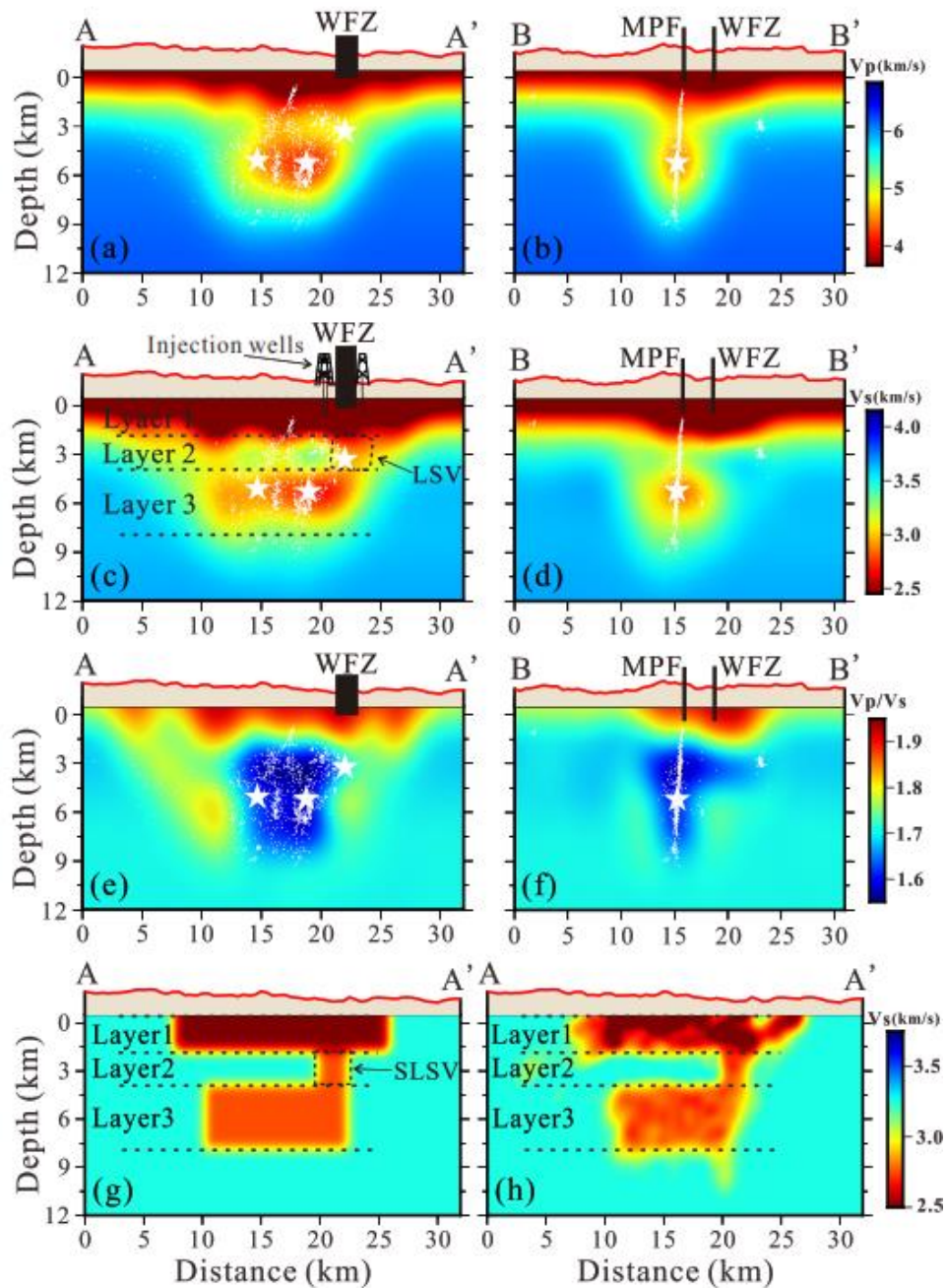
178 To further investigate whether the three-layer upper crustal structure discussed above is a  
179 robust feature, we apply a synthetic reconstruction test based on a simplified 3D  $V_s$  model of the  
180 study area (Figure 3g, h). The synthetic model has a background  $V_s$  of 3.25 km/s, and consists of  
181 a low-velocity anomaly of 2.5 km/s from the surface to 1.5 km in "Layer 1", another low-velocity  
182 anomaly of "2.75" km/s at 3.5-8 km depth in "Layer 3", and a narrow cylindrical low-velocity  
183 anomaly of 2.75 km/s that connects "Layer 1" and "Layer 3" near the northwest edge of the  
184 anomalies (marked as "SLSV" in Figure 3g). We generate synthetic travel time data based on the  
185 source-receiver geometry, and obtain inverted velocity model following the same workflow. The  
186 inverted model agrees well with the input model in terms of both the shape and amplitude of the  
187 velocity anomalies (Figure 3h), suggesting that the layered structure is a robust feature. A similar  
188 input model without the "SLSV" feature was also tested, which further ensures that the recovered  
189 "SLSV" in Figure 3h was not an artifact caused by smearing effects (Figure S9).



190

191 **Figure 2.** Map views of the final velocity models:  $V_p$  (left),  $V_s$  (middle), and  $V_p/V_s$  (right). Black  
 192 lines mark the faults in study area and the two profiles are shown as red lines on Figure 2a. White  
 193 dots are projected earthquakes from the relocated catalog using 3D velocity models within 1.5 km  
 194 of the depth slices.

195



196 **Figure 3.** (a-f) Cross section along profiles AA' (left) and BB' (right). Top, middle, and bottom  
 197 panels show the  $V_p$ ,  $V_s$ , and  $V_p/V_s$ , respectively. White dots are projected earthquakes from the  
 198 relocated catalog using 3D velocity models within 1.5 km of the cross sections and the Mw 5.7  
 199 mainshock, Mw 4.8 foreshock and Mw 4.8 aftershock are shown as white stars. (g) Synthetic input  
 200 model with three layers. (h) Inverted model for the synthetic test.

201

## 202 4 Discussion

203 Induced earthquakes are generally interpreted as the reactivation of pre-existing faults due  
204 to stress changes caused by fluid injection (Ellsworth, 2013; Gupta, 2002). Thus, the detailed  
205 structure and morphology of the MPF is important for understanding induced seismicity in Prague.  
206 WFZ is the most significant mapped fault system near the Prague area, but the distribution of  
207 earthquakes (Figures 1, 2) suggests that the unmapped NE-oriented MPF, instead of the WFZ, is  
208 the primary host of the 2011 Prague sequence (Keranen et al., 2013; McMahon et al., 2017).  
209 Aeromagnetic Data reveals a correlation between low magnetic anomalies and MPF with strong  
210 heterogeneities within the fault zone (Shah & Crain, 2018). Yet, there has been no high-resolution  
211 tomographic studies to date at local scale to constrain the detailed morphology of MPF and its  
212 relationship with the Prague sequence.

213 Velocity variations in fault zones reflect the combined effects of lithology, crack density,  
214 porosity, and water content (e.g., He et al., 2018; Langenbruch & Zoback, 2016). Based on our 3D  
215 relocation of earthquakes (Figure S10) and velocity models, we infer that the MPF has a strike of  
216 about N45°E (Figure 2), which is consistent with the orientation of the MPF suggested by the  
217 aftershock distribution (McMahon et al., 2017). The 3D velocity models show near-vertical, low-  
218 velocity zones (Figures 3b, d) with low Vp/Vs (Figure 3f) occurring between 2.5 km and 8 km  
219 depth, coincident with the coseismic rupture of the mainshock and spatial extent of the aftershocks.  
220 In addition, the vertical variations of the velocity and Vp/Vs structures (e.g., "Layer 2" versus  
221 "Layer 3" in Figure 3c) suggest that small-scale complexities do exist within the fault zone, as  
222 previously recognized by Shah and Crain (2018). It should be noted that our model has a spatial  
223 resolution of ~2.5 kilometers, which prevents the identification of minor fault structures, such as  
224 the EW-trending fault branch outlined by the aftershocks of the Mw 4.8 aftershock on 8 November  
225 2011 (Cochran et al., 2020; McMahon et al., 2017).

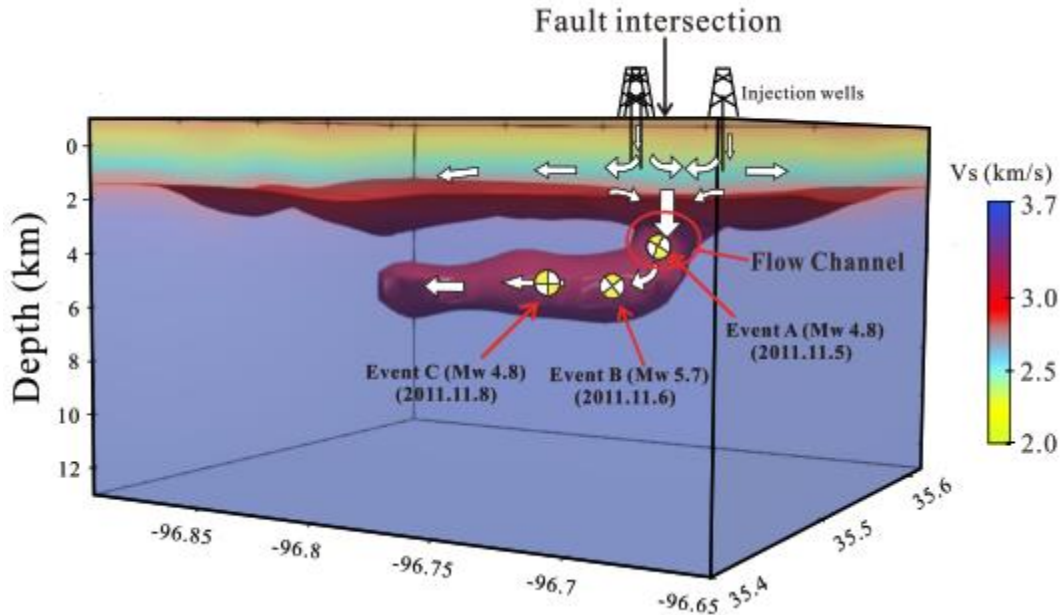
226 McMahon et al. (2017) shows that over 99.9% of the cumulative moment in the catalog  
227 was released below 2.6 km depth. Our updated earthquake relocations using 3D velocity models  
228 (Figures 2, 3 and S10) show that most earthquakes (including the Mw 5.7 mainshock) occurred  
229 within the imaged velocity anomalies. The 3D relocations are overall consistent with 1D  
230 relocations with relatively small changes, however, both 3D and 1D relocations show large shifts  
231 from the original locations (Figure S11). More significantly, all the larger earthquakes in this  
232 sequence ( $M_w \geq 3.5$ ) occurred at depths of ~4-9 km of the MPF (Figure S12). Earthquake scaling  
233 laws indicate that these larger earthquakes could have been produced by a fault with the size of  
234 the MPF imaged by this study (e.g., Qin et al., 2019; Walsh & Zoback, 2015).

235 The shear and bulk modulus are different for saturated cracks with different aspect ratios,  
236 and the Vp/Vs anomalies can be related to different factors including water content, aspect ratio,  
237 and crack density (Lin & Shearer, 2009; Shearer, 1988). Our tomographic models reveal prominent  
238 high Vp/Vs in the sedimentary layer ("Layer 1" in Figure 3c), where large volume of wastewater  
239 has been injected into the Arbuckle group (Keranen et al., 2013), suggesting that the sedimentary  
240 layer is characterized by fluid-filled cracks with small aspect ratio in saturated carbonates (e.g.,  
241  $< 0.01$ , Lin and Shearer, 2009; Shearer, 1988). The "Layer 2" has normal granite velocity values  
242 and relatively normal Vp/Vs, which indicates a relatively uniform structure and lower  
243 permeability. The intersection of the MPF and WFZ is marked as a low shear velocity zone,  
244 possibly indicating reduced fault strength.

245 The  $V_p/V_s$  at the MPF ("Layer 3" in Figure 3c) is approximately 1.6, which is around 8%  
246 lower than the background value of 1.73. This can be explained by fluid-filled cracks with high  
247 aspect ratio (Shearer, 1988; Takei, 2002). A 8% reduction in the  $V_p/V_s$  corresponds to a medium  
248 porosity of around 10% assuming an aspect ratio of 0.1 and an initial  $V_p/V_s$  of 1.73 (Lin & Shearer,  
249 2009). Moreover, we apply the method of Lin and Shearer (2007) to estimate the situ  $V_p/V_s$  in  
250 "Layer 3" using P-wave and S-wave differential times (Figure S13, Text S3). This technique has  
251 high resolution for near-source  $V_p/V_s$  using high-precision differential times and a robust misfit  
252 function method. The consistency between the  $V_p/V_s$  (~1.6) estimated using differential travel-  
253 times and our tomography results highlights the reliability of our  $V_p/V_s$  estimates.

254 Due to the lack of seismicity and monitoring stations prior to the Prague sequence, it is  
255 impossible to infer the structure in earlier stage so as to provide a definite triggering process of the  
256 Prague sequence. Our 3D model represents the average upper crust structure during and following  
257 the Prague earthquake sequence. Figure 4 shows a 3D perspective view of the inverted  $V_s$  model.  
258 The isosurface of a  $V_s$  of 3 km/s forms a cylinder at depths of ~3.5-8 km, outlining the extent of  
259 the low-velocity "Layer 3" that extends upwards and connects to the sedimentary layer through a  
260 possible flow channel near the intersection of WFZ and MPF. Additional plots (Figures S14 and  
261 S15) and animations showing the 3D  $V_s$  isosurface structure from various viewing angles are  
262 included in the Supporting Information. Lateral variations of body wave velocities are widely  
263 observed worldwide in fault zones, whether associated with industrial activity or not, and are often  
264 related to fluids (Allam et al., 2014; Di Stefano et al., 2011; Lei & Zhao, 2009; Tan et al., 2020).  
265 In the current study, the resolved strong velocity and  $V_p/V_s$  anomalies at seismogenic depths  
266 define the extent of the possibly overpressurized volume influenced by fluid injection, which  
267 suggests that fluid-filled cracks may be present down at least 8 km in depth, and therefore, fluid  
268 may have played a key role in triggering the sequence.

269 Combining all the observations, we propose a simplified conceptual model for the  
270 development of the Prague sequence: Fluid injection into the three active injection wells within  
271 ~1.5 km of Event A (Figure 1) started since 1993, and extended into the deeper Arbuckle Group  
272 between ~1.3 and 2.1 km depth (Keranen et al., 2013). Since the Arbuckle Group comprises highly  
273 permeable reservoirs (Keranen et al., 2013), the wastewater quickly diffused into the surroundings  
274 (Shah & Keller, 2017), triggering some small earthquakes due to the increase in pore pressure. The  
275 relatively complete central Oklahoma granite group ("Layer 2" in Figure 3c, Shah & Keller, 2017)  
276 at depth ~1.5-3.5 km, which has a very low permeability, inhibits further downward wastewater  
277 penetration in general. Seismicity during this time period is therefore limited to the sedimentary  
278 layers and the uncovered preexisting MPF remains stable. The low-permeability of "Layer 2"  
279 maybe the main reason that the first sizeable earthquake did not occur until 18 years after the  
280 wastewater injection commenced (Keranen et al., 2013). As noted by Keranen & Weingarten  
281 (2018), the lack of induced seismicity in North Dakota is partially due to the low permeable layers  
282 above and below the injection layer, which supports our interpretation. However, as injection  
283 continues, at the intersection of the MPF and WFZ in "Layer 2" (marked as "LSV" in Figure 3c),  
284 the fault strength gradually decreases in response to increased pore pressure as wastewater  
285 accumulates. Then the density-driven pressure front migrates downward (Pollyea, et al., 2019) at  
286 this fault intersection. This process of downward diffusion resulted in increased pore pressure,  
287 decrease the fault strength, and may have induced the Mw 4.8 foreshock (Event A in Figure 4) in  
288 "Layer 2" (Keranen et al., 2013; Sumy et al., 2014).



289  
290

291 **Figure 4.** 3D visualization of the inverted Vs model. The isosurface of a Vs 3 km/s forms a cylinder  
292 at the depth of ~3.5-8 km and connects upward with the shallow part near in the fault intersection.  
293 The magnitude and location of Event A (Mw 4.8, at 3.1 km depth), B (Mw 5.7, at 5.2 km depth)  
294 and C (Mw 4.8, at 5.0 km depth) are from USGS. The white arrows indicate possible directions of  
295 fluid diffusion and the red circle marks the possible location of the flow channel.

296

297 The MPF is optimally oriented in the local stress field, and may have been critically  
298 stressed (Cochran et al., 2020; Qin et al., 2019). The stress interactions from foreshocks and  
299 accumulated pore pressure triggered a run-off rupture along the MPF, resulting in the Mw 5.7  
300 mainshock (Event B in Figure 4). Numerical modeling suggests that critically stressed faults is  
301 more likely to have run-off ruptures that extends beyond pressurized zone (Gischig, 2015).

302 The rupture processes of Event A and B might have created a flow channel in "Layer 2"  
303 (Figure 4), allowing the wastewater to easily penetrate into the MPF. Subsequently, the combined  
304 effect of the Coulomb stress changes from Events A and B and the increased pore pressure  
305 promotes the failure of the Mw 4.8 aftershock (Event C in Figure 4) and later aftershocks (Sumy  
306 et al., 2014).

307 Based on our model, the low permeability of "Layer 2" and the limited pathway at the fault  
308 intersection for the downward fluid penetration are the two reasons for the significant delay of the  
309 first sizeable earthquake that occurred 18 years after the fluid injection started. An in-depth study  
310 of Layer 2, including assessment of lateral differences in lithology and structure, will be critical in  
311 understanding the triggering processes of the Prague sequence. In addition, smaller scale structures  
312 are evident but beyond the resolution of our tomographic models. Most of those secondary faults  
313 including the ones that hosted the Mw 4.8 foreshock and Mw 4.8 aftershock were found not  
314 optimally oriented for failure in the local stress field, which underlines the dominant effect of  
315 elevated pore fluid pressures, when compared with the small footprint of stress perturbations

316 caused by static and dynamic stress transfers (Brown et al., 2018), in promoting failure along those  
317 smaller faults that would otherwise remain inactivated in ambient stress field (Cochran et al.,  
318 2020). Our proposed conceptual model can provide valuable guidance for numerical simulations  
319 on induced seismicity with a particular target on the delayed mainshock occurrence as observed at  
320 Prague and the 2017 Mw 5.5 Pohang, Korea earthquake (Yeo et al., 2020)

## 321 **5 Conclusions**

322 In this study, we imaged fine upper crustal velocity structures in the fault zone of the 2011  
323 Mw 5.7 Prague, Oklahoma earthquake using data from a dense local seismic network. The new  
324 models reveal a three-layer structure of the Prague fault zone: a sedimentary layer extending from  
325 the surface to a depth of ~1.5 km, comprised of fluid-filled cracks with small aspect ratio, followed  
326 underneath by a relatively uniform basement layer with low permeability at around 1.5-3.5 km  
327 depths, and then a layer in the basement with fluid-filled cracks of high aspect ratio at depths of  
328 around 3.5-8 km. Based on our obtained velocity models and relocated earthquake locations, we  
329 infer that the MPF ruptured in "Layer 3" and hosted the majority of the larger events in the Prague  
330 sequence including the Mw 5.7 mainshock. The low permeability of "Layer 2" is probably what  
331 delays the first sizeable earthquake (Mw 4.8 foreshock) after 18 years of wastewater injection.  
332 More importantly, the weak zone at the fault intersection had provided the focused pathway for  
333 the downward penetration of the injected fluids.

## 334 **Acknowledgments**

335 We are grateful to Dr. Zenonos for providing us the software to invert  $V_p/V_s$ . We thank  
336 the Editor Dr. Germán Prieto, the anonymous Associate Editor, and two anonymous reviewers for  
337 helpful reviews. This study was supported by USGS NEHRP grant G18AP00022. Figures were  
338 made using GMT (Wessel et al., 2019), Matplotlib (Hunter, 2007) and ParaView. The seismic  
339 waveforms were obtained from the Incorporated Research Institutions for Seismology (IRIS) Data  
340 Management Center ([http://ds.iris.edu/wilber3/find\\_event](http://ds.iris.edu/wilber3/find_event)).

## 341 **Open Research**

342 The data used and produced in this study including the phase picks, relocated catalog,  
343 inverted velocity models are available at <https://zenodo.org/record/5501768>.

## 344 **References**

- 345 Allam, A. A., Ben-Zion, Y., Kurzon, I., & Vernon, F. (2014). Seismic velocity structure in the Hot  
346 Springs and trifurcation areas of the San Jacinto Fault zone, California, from double-difference  
347 tomography. *Geophysical Journal International*, 198(2), 978-999.  
348 <https://doi.org/10.1093/gji/ggu176>
- 349 Brown, M. R. M., & Ge, S. (2018). Small earthquakes matter in injection-induced seismicity.  
350 *Geophysical Research Letters*, 45, 5445-5453. <https://doi.org/10.1029/2018GL077472>
- 351 Chai, C., Delorey, A. A., Maceira, M., Levandowski, W., Guyer, R. A., Zhang, H., et al. (2021).  
352 A 3D Full Stress Tensor Model for Oklahoma. *Journal of Geophysical Research: Solid Earth*,  
353 126(4), e2020JB021113. <https://doi.org/10.1029/2020JB021113>

- 354 Chen, X., Nakata, N., Pennington, C., Haffener, J., Chang, J. C., and He, X. (2017). The Pawnee  
355 earthquake as a result of the interplay among injection, faults and foreshocks. *Scientific Reports*,  
356 7(1), 4945. <https://doi.org/10.1038/s41598-017-04992-z>
- 357 Chiarabba, C., De Gori, P., Cattaneo, M., Spallarossa, D., & Segou, M. (2018). Faults geometry  
358 and the role of fluids in the 2016–2017 Central Italy seismic sequence. *Geophysical Research*  
359 *Letters*, 45, 6963–6971. <https://doi.org/10.1029/2018GL077485>
- 360 Cochran, E. S., Skoumal, R. J., McPhillips, D., Ross, Z. E., & Keranen, K. M. (2020), Activation  
361 of optimally and unfavourably oriented faults in a uniform local stress field during the 2011  
362 Prague, Oklahoma, sequence. *Geophysical Journal International*, 222, 153-168.  
363 <https://doi.org/10.1093/gji/ggaa153>
- 364 Di Stefano, R., Chiarabba, C., Chiaraluce, L., Cocco, M., De Gori, P., Piccinini, D., & Valoroso,  
365 L. (2011). Fault zone properties affecting the rupture evolution of the 2009 (Mw 6.1) L'Aquila  
366 earthquake (central Italy): Insights from seismic tomography. *Geophysical Research Letters*,  
367 38(10). <https://doi.org/10.1029/2011gl047365>
- 368 de Kool, M., Rawlinson, N., and Sambridge, M. (2006). A practical grid based method for tracking  
369 multiple refraction and reflection phases in 3D heterogeneous media. *Geophysical Journal*  
370 *International*, 167, 253-270.
- 371 Ellsworth, W. L. (2013). Injection-induced earthquakes. *Science*, 341, 142–149.
- 372 Frohlich C, Hayward C, Stump B, & Potter E. (2011). The Dallas-Fort Worth earthquake sequence:  
373 October 2008 through May 2009. *Bull. Seismol. Soc. Am.*, 101:327–40
- 374 Gischig, V. S. (2015). Rupture propagation behavior and the largest possible earthquake induced  
375 by fluid injection into deep reservoirs. *Geophysical Research Letters*, 42, 7420-7428.  
376 [doi:10.1002/2015GL065072](https://doi.org/10.1002/2015GL065072)
- 377 Gupta, H. K. (2002). A review of recent studies of triggered earthquakes by artificial water  
378 reservoirs with special emphasis on earthquakes in Koyna, India. *Earth-Science Reviews*, 58(3-4),  
379 279–310. [https://doi.org/10.1016/S0012-8252\(02\)00063-6](https://doi.org/10.1016/S0012-8252(02)00063-6)
- 380 He, L., Sun, X., Yang, H., Qin, J., Shen, Y., & Ye, X. (2018). Upper crustal structure and  
381 earthquake mechanism in the Xinfengjiang Water Reservoir, Guangdong, China. *Journal of*  
382 *Geophysical Research: Solid Earth*, 123. <https://doi.org/10.1029/2017JB015404>
- 383 Horton S. (2012). Disposal of Hydrofracking Waste Fluid by Injection into Subsurface Aquifers  
384 Triggers Earthquake Swarm in Central Arkansas with Potential for Damaging Earthquake.  
385 *Seismological Research Letters*, 83(2), 250-260.
- 386 Hunter, J. D.: Matplotlib: A 2D Graphics Environment. *Computing in Science & Engineering*,  
387 9(3), (2007), 90-95.
- 388 Keranen, K. M., H. M. Savage, G. A. Abers, & E. S. Cochran. (2013). Potentially induced  
389 earthquakes in Oklahoma, USA: Links between wastewater injection and the 2011 Mw 5.7  
390 earthquake sequence. *Geology*, 2011-2014, G34045, [doi:10.1130/G34045.1](https://doi.org/10.1130/G34045.1).
- 391 Keranen, K. M. & Weingarten, M. (2018). Induced Seismicity. *Annual Review of Earth and*  
392 *Planetary Sciences*, 46, 149-174.

- 393 Langenbruch, C., & M. D. Zoback. (2016). How will induced seismicity in Oklahoma respond to  
394 decreased saltwater injection rates?. *Sci. Adv.*, 2(11), e1601542. doi:10.1126/sciadv.1601542
- 395 Lei, J., & D. Zhao. (2009). Structural heterogeneity of the Longmenshan fault zone and the  
396 mechanism of the 2008 Wenchuan earthquake (Ms 8.0). *Geochem. Geophys. Geosyst.*, 10,  
397 Q10010. doi:10.1029/2009GC002590
- 398 Lin, G., & Shearer, P. M. (2007). Estimating Local Vp/Vs Ratios within Similar Earthquake  
399 Clusters. *Bulletin of the Seismological Society of America*, 97(2), 379-388.  
400 doi:10.1785/0120060115
- 401 Lin, G., & Shearer, P. M. (2009). Evidence for water-filled cracks in earthquake source regions.  
402 *Geophysical Research Letters*, 36, L17315. <https://doi.org/10.1029/2009GL039098>
- 403 McMahan, N. D., R. C. Aster, W. L. Yeck, D. E. McNamara, & H. M. Benz. (2017). Aftershock  
404 catalog for the November 2011 Prague, Oklahoma, earthquake sequence, U.S. Geol. Surv. Data  
405 Release, doi:10.5066/F7FJ2FNT.
- 406 Pei, S., Peng, Z., & Chen, X. (2018). Locations of injection-induced earthquakes in Oklahoma  
407 controlled by crustal structures. *Journal of Geophysical Research: Solid Earth*, 123, 2332-2344.  
408 <https://doi.org/10.1002/2017JB014983>
- 409 Pennington C.N., Chen X., Abercrombie R.E., & Wu Q. (2021). Cross Validation of Stress Drop  
410 Estimates and Interpretations for the 2011 Prague, OK, Earthquake Sequence Using Multiple  
411 Methods. *Journal of Geophysical Research: Solid Earth*, 126, e2020JB020888.  
412 <https://doi.org/10.1029/2020JB020888>
- 413 Petersen MD, Mueller CS, Moschetti MP, Hoover SM, Llenos AL, et al. (2016). Seismic-hazard  
414 forecast for 2016 including induced and natural earthquakes in the central and eastern United  
415 States. *Seismol. Res. Lett.*, 87:1327-1341
- 416 Petersen MD, Mueller CS, Moschetti MP, Hoover SM, Shumway AM, et al. (2017). 2017 One-  
417 Year Seismic-Hazard Forecast for the Central and Eastern United States from Induced and Natural  
418 Earthquakes. *Seismol. Res. Lett.*, 88:772-783
- 419 Petersen MD, Mueller CS, Moschetti MP, Hoover SM, & Rukstales KS. (2018), 2018 One-Year  
420 Seismic Hazard Forecast for the Central and Eastern United States from Induced and Natural  
421 Earthquakes. *Seismol. Res. Lett.*, 89:1049-1061
- 422 Pollyea, R.M., Chapman, M.C., Jayne, R.S., & Wu, H. (2019). High density oilfield wastewater  
423 disposal causes deeper, stronger, and more persistent earthquakes. *Nature communications*, 10(1),  
424 1-10.
- 425 Qin, Y., Chen, X., Walter, J. I., Haffener, J., Trugman, D. T., Carpenter, B. M., et al. (2019).  
426 Deciphering the stress state of seismogenic faults in Oklahoma and southern Kansas based on an  
427 improved stress map. *Journal of Geophysical Research: Solid Earth*, 124(12), 12920-12934.  
428 <https://doi.org/10.1029/2019JB018377>
- 429 Rawlinson, N., Kool, M. D., & Sambridge, M. (2006). Seismic wavefront tracking in 3D  
430 heterogeneous media: Applications with multiple data classes. *Exploration Geophysics*, 37(4),  
431 322–330. <https://doi.org/10.1071/eg06322>
- 432 Takei, Y. (2002). Effect of pore geometry on Vp/Vs: From equilibrium geometry to crack. *Journal*  
433 *of Geophysical Research*, 107(B2), 2043. <https://doi.org/10.1029/2001JB000522>

- 434 Tan, Y., Hu, J., Zhang, H., Chen, Y., Qian, J., Wang, Q., et al. (2020). Hydraulic fracturing induced  
435 seismicity in the southern Sichuan Basin due to fluid diffusion inferred from seismic and injection  
436 data analysis. *Geophysical Research Letters*, 47. <https://doi.org/10.1029/2019GL084885>
- 437 Schultz R, Corlett H, Haug K, Kocon K, MacCormack K, et al. (2016). Linking fossil reefs with  
438 earthquakes: geologic insight to where induced seismicity occurs in Alberta. *Geophys. Res. Lett.*,  
439 43:2534-42
- 440 Shah, A. K., & Keller, G. R. (2017). Geologic influence on induced seismicity: Constraints from  
441 potential field data in Oklahoma. *Geophysical Research Letters*, 44, 152-161.  
442 <https://doi.org/10.1002/2016GL071808>
- 443 Shah, A. K., & Crain, K. (2018). Aeromagnetic Data Reveal Potential Seismogenic Basement  
444 Faults in the Induced Seismicity Setting of Oklahoma. *Geophysical Research Letters*, 45, 5948-  
445 5958. <https://doi.org/10.1029/2018GL077768>
- 446 Shearer, P. M. (1988). Cracked media, Poisson's ratio, and the structure of the upper oceanic crust.  
447 *Geophys. J.*, 92, 357- 362.
- 448 Stewart FL, & Ingelson A. (2017). Regulating energy innovation:US responses to hydraulic  
449 fracturing, wastewater injection and induced seismicity. *J. Energy Nat. Resour. Law*, 35:109-46
- 450 Sumy, D.F., Cochran, E.S., Keranen, K.M., Wei, M., & Abers, G.A. (2014). Observations of static  
451 Coulomb stress triggering of the November 2011 M 5.7 Oklahoma earth-quake sequence. *J.*  
452 *Geophys. Res., Solid Earth*, 119, 1904-1923.
- 453 Sumy, D. F., Neighbors, C. J., Cochran, E. S., & Keranen, K. M. (2017). Low stress drops observed  
454 for aftershocks of the 2011 M w 5.7 Prague, Oklahoma, earthquake. *Journal of Geophysical*  
455 *Research: Solid Earth*, 122(5), 3813-3834. <https://doi.org/10.1002/2016JB013153>
- 456 Sun, X., & Hartzell, S. (2014). Finite-fault slip model of the 2011 Mw 5.6 Prague, Oklahoma  
457 earthquake from regional waveforms. *Geophysical Research Letters*, 41(12), 4207-4213.  
458 <https://doi.org/10.1002/2014GL060410>
- 459 Yeck, W. L., M. Weingarten, H. M. Benz, D. E. Mcnamara, E. Bergman, R. B. Herrmann, J.  
460 Rubinstein, & P. S. Earle. (2016). Far-field pressurization likely caused one of the largest  
461 injection induced earthquakes by reactivating a large pre-existing basement fault structure.  
462 *Geophys. Res. Lett.*, 43(10),198-10,207. doi:10.1002/2016GL070861
- 463 Yeo, I. W., Brown, M. R. M., Ge, S., & Lee, K. K. (2020). Causal mechanism of injection-induced  
464 earthquakes through the Mw 5.5 Pohang earthquake case study. *Nature Communications*, 11(1),  
465 2614. <https://doi.org/10.1038/s41467-020-16408-0>
- 466 Waldhauser, F., & Ellsworth, W. L. (2000). A doubleDifference earthquake location algorithm:  
467 Method and application to the northern Hayward fault, California. *Bulletin of the Seismological*  
468 *Society of America*, 90(6), 1353-1368. <https://doi.org/10.1785/0120000006>
- 469 Walsh, F., & Zoback, M. D. (2015). Oklahoma's recent earthquakes and saltwater disposal.  
470 *Science Advances*, 1(5), e1500195. <https://doi.org/10.1126/sciadv.1500195>
- 471 Wessel, P., Luis, J. F., Uieda, L., Scharroo, R., Wobbe, F., Smith, W. H. F., & Tian, D. (2019).  
472 The Generic Mapping Tools version 6. *Geochemistry, Geophysics, Geosystems*, 20, 5556–5564.  
473 <https://doi.org/10.1029/2019GC008515>

- 474 Wu, Q., Chapman, M., & Chen, X. (2018). Stress-drop variations of induced earthquakes in  
475 Oklahoma. *Bulletin of the Seismological Society of America*, 108(3), 1107-1123.  
476 <https://doi.org/10.1785/0120170335>
- 477 Zenonos, A., DeSiena, L., Widiyantoro, S., Rawlinson, N. (2020). Direct inversion of S-P  
478 differential arrival times for Vp/Vs ratio in SE Asia. *Journal of Geophysical Research: Solid*  
479 *Earth*, 125, e2019JB019152. <https://doi.org/10.1029/2019JB019152>